Silicon mediated twin formation in laser direct energy deposited 316L stainless steel

Kewei Chen, Juan Guillermo Santos Macías, Nathalie Isac, Maxime Vallet, Louis Cornet, Manas V Upadhyay

Silicon mediated twin formation in laser direct energy deposited 316L stainless steel

Kewei Chen[a], Juan Guillermo Santos Macías[a,1], Nathalie Isac[a], Maxime Vallet[b, c], Louis Cornet[b], Manas V. Upadhyay[a, *]

[a] *Laboratoire de Mécanique des Solides (LMS), Ecole Polytechnique, Institut Polytechnique de Paris, CNRS UMR 7649, Palaiseau 91128, France*

[b] *Université Paris-Saclay, CentraleSupélec, ENS Paris-Saclay, CNRS, LMPS - Laboratoire de Mécanique Paris-Saclay, 91190 Gif-sur-Yvette, France*

[c] *Université Paris-Saclay, CentraleSupélec, CNRS, Laboratoire SPMS - Structures, Propriétés et Modélisation des Solides, 91190 Gif-sur-Yvette, France*

[*]Corresponding author: *manas.upadhyay@polytechnique.edu*

Abstract

Microstructures of two laser direct energy deposited 316L stainless steel samples printed using the same additive manufacturing parameters and primarily differing in their Si content, 2.2wt% (316L-Si) and 0.73wt% (316L), were studied. A larger length fraction of Σ3 twin boundaries (~23% of all boundaries in austenite) was observed in 316L-Si than in 316L (~2%). The twin-related domains in 316L-Si are attributed to two mechanisms: (i) icosahedral short-range order-mediated nucleation in the melt based on observation of grain clusters sharing a common <110> fivefold symmetry axis, and (ii) massive transformation from ferrite to austenite, confirmed by the presence of refined grains, absence of solidification cells and jagged boundaries between austenite grains. For the same printing parameters, massive transformation occurs in 316L-Si due to a higher equivalent chromium to equivalent nickel ratio (1.73) than in 316L (1.46). Thus, twin boundary fractions in additively manufactured 316L can be increased via Si addition.

Keywords: *Twins, additive manufacturing, stainless steel, ISRO, massive transformation*

[1] Current address: IMDEA materials institute, Eric Kandel 2, Tecnogetafe-Getafe 28906, Spain

Additive manufacturing (AM) of 316L stainless steel has garnered attention for its ability to enhance strength, owing to its distinctive microstructure resulting from rapid heating and cooling during fabrication [1–5]. However, specific applications, e.g., in marine and medical, necessitate resistance to intergranular corrosion and stress corrosion cracking [6–8], which can be achieved through a high proportion of low coincident site lattice ($3\leq\sum\leq9$) grain boundaries (GBs) [9–16].

One method to generate low-$\sum$ GBs in AM 316L is thermomechanical processes that continuously trigger recrystallization [17]. However, applying this approach to AM 316L would lead to undesirable geometry changes. Another approach involves annealing of AM 316L to trigger recrystallization and formation of annealing twins possibly via the strain-induced boundary migration mechanism [18,19]. This method typically results in undesirably large grains [20,21], which are detrimental to mechanical properties. Recently, Monier *et al.* [22] demonstrated a third approach to achieve a large number of twins in laser-based powder bed fused (L-PBF) 316L by icosahedral short-range order (ISRO)-mediated nucleation mechanism, as evidenced by common <110> fivefold symmetry axes of neighboring twins.

ISRO-mediated nucleation is explained in detail in a recent work by Rappaz *et al.* [23] and briefly recalled here. A regular icosahedron possesses 20 equilateral triangular facets, 12 vertices and 30 edges. The axes connecting opposite vertices represent fivefold symmetry axes. The nucleation process involves the following steps: 1) initial formation of ISRO motifs around specific solutes in the liquid; 2) aggregation of these motifs into icosahedral quasicrystals (in some instances, this step may not occur [23,24]); 3) occurrence of heteroepitaxy between the face-centered cubic (FCC) phase and the icosahedral quasicrystals (or ISRO motifs in the initial step) via {111} planes and <110> directions, resulting in the formation of twins and multiple-twin relationships between nearest-neighbor grains [23]. ISRO-mediated nucleation has been reported in L-PBF FCC metals including Al alloys [25,26], commercially pure Ni [27] and 316L [22]. However, until very recently [28] this mechanism had not been reported in powder-based laser directed energy deposition (L-DED) FCC alloys, whose relatively lower undercooling due to the slower cooling rate (maximum between 10^2 and 10^5 K/s [29]) with respect to their L-PBF counterparts (maximum between 10^6 and 10^7 K/s [30]) is expected to be unfavorable for the formation of ISRO motifs and/or icosahedral quasicrystals [31,32].

In this work, the aim is to increase the amount of twin boundaries in L-DED 316L by increasing the Si content in 316L with the expectation that it promotes nucleation of ISRO motifs. Increasing the Si content is a good candidate because i) based on Rappaz *et al*. [23] and some references therein, achieving a close-packed ISRO structure necessitates an atom at the center being ~0.902 times the size of atoms at the twelve vertices. In the case of 316L, the closest that one can arrive to this size ratio is by alloying with Si; the covalent atomic radius ratio between Si (1.11 Å) and Fe (1.32 Å) is approximately 0.84 [33]. However, size ratio by itself may not be a sufficient condition. ii) It has been reported that both Si and Fe atoms can form Fe-centered ISRO motifs [34]; furthermore, Si can substitute Fe atoms at the vertices, increasing the

probability of forming such motifs after addition of Si [34]. iii) Si is a wetting-favorable element [35] and adding Si should avoid hot cracking during L-DED.

To test this hypothesis, L-DED samples were fabricated from powders with two different compositions of 316L varying mainly in Si content. Both powders, with a particle size ranging from 45 to 90 μm, were manufactured via inert gas atomization by Oerlikon GmbH (Germany). These powders were used to print cube-shaped samples with dimensions of 15×15×15 mm^3 using a BeAM Modulo 400 L-DED machine equipped with a 500W YLR-fiber laser. The printing process employed a bidirectional scanning strategy with a 90º laser direction rotation between layers. Same printing parameters were used for both powders: power 250 W, scanning speed 1800 mm/min, powder flow rate 6.8 g/min, track overlap 40%, and vertical displacement of focusing head 0.12 mm after each layer deposition. Table 1 shows the compositions of the two as-built samples measured using inductively coupled plasma spectroscopy and total organic carbon analysis (FiLAB, France). The composition of the first part is 316L with 0.73wt% Si (316L), which is within the range (< 1wt%) of typical Si content in this steel, and of the second part is 316L with 2.20wt% Si (316L-Si).

Table 1. Composition of 316L and 316L-Si parts

As-built parts / Composition	Fe	C	S	N	O	P	Si	Mn
316L-Si	Bal.	0.020	0.005	0.080	0.014	0.008	**2.20**	0.64
316L	Bal.	0.018	0.005	0.083	0.024	0.012	**0.73**	1.40
As-built parts / Composition	Ni	Cr	Cu	Mo	Co	Ti	B	
316L-Si	12.2	17.4	0.031	3.0	0.052	<0.005	0.003	
316L	13.3	18.7	0.063	2.4	0.026	<0.005	0.007	

The front sides (plane composed of building + printing directions) of the two samples were ground using #320, 500, 1200, 2400 and 4000 SiC papers, followed by polishing with 3 μm and 1 μm diamond paste. For electron backscatter diffraction (EBSD) observations, specimens were subjected to additional polishing using a Buehler vibratory polisher. For microsegregation structure examination, samples were etched using 10% (w/v) oxalic acid aqueous solution for 15 seconds. EBSD scans were performed on the top (Figure 1a), middle, and bottom (Figure S1) areas using an Oxford symmetry detector in an FEI Helios 600 scanning electron microscope (SEM).

For transmission electron microscopy (TEM) observations, thin lamellae were extracted using an FEI Helios Nanolab 660 SEM equipped with a focused ion beam. Energy dispersive X-ray spectroscopy (EDS) and high-angle annular dark-field (HAADF) images were then acquired using an aberration-corrected FEI Titan^3 G2 TEM. In addition, transmission Kikuchi diffraction (TKD) maps of TEM lamellae were obtained using the FEI 600 SEM.

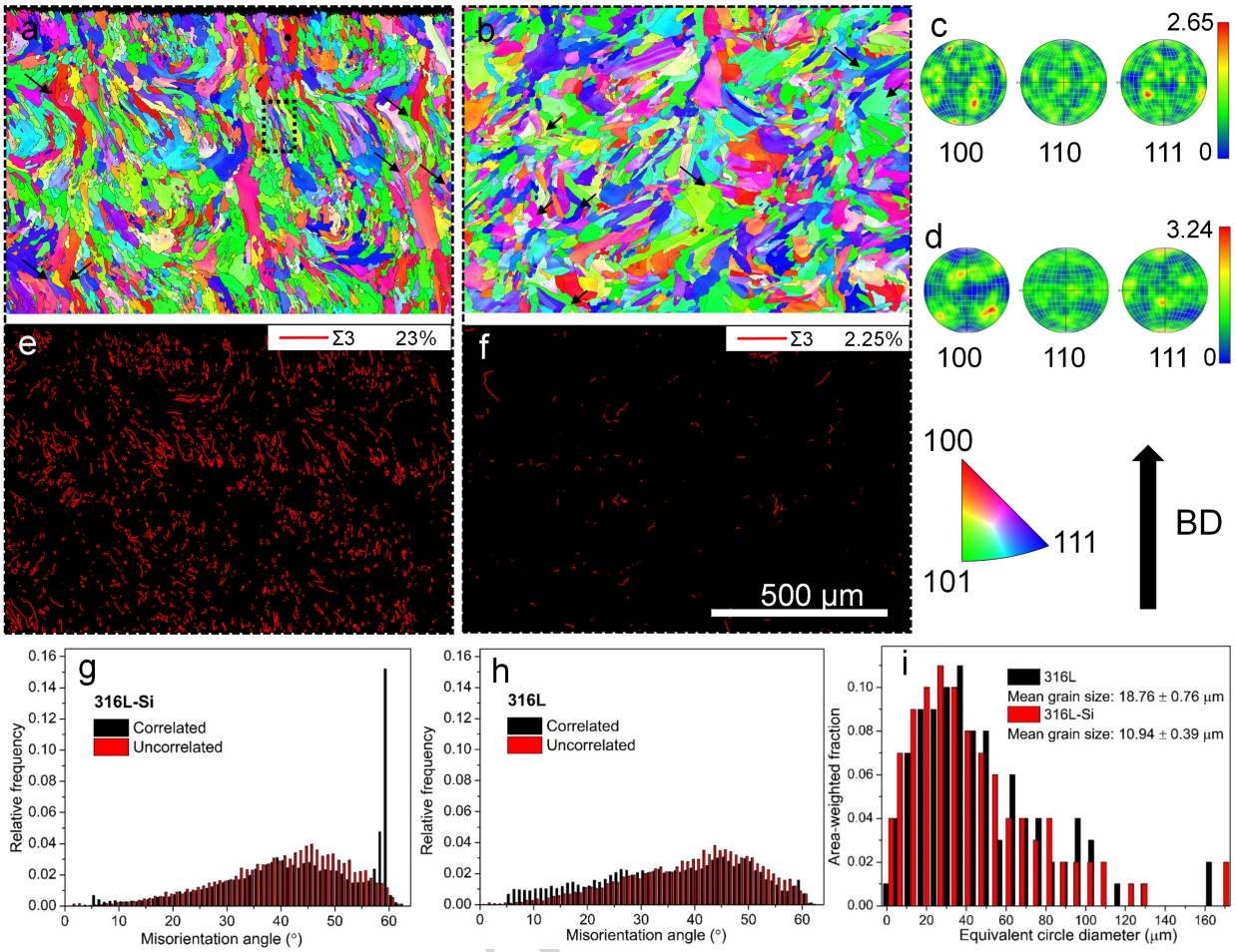

Figure 1. (a, b) EBSD IPF maps along building direction (BD) and (e, f) ∑3 twin boundary maps of top areas of the polished surface of as-built (a, e) 316L-Si and (b, f) 316L samples with 0.5 μm scanning step size. The length fractions of ∑3 twin boundaries are inserted in (e, f) and the scale bar for (a, b, e and f) is shown in (f). Pole figures (c) and (d) correspond to areas in (a) and (b), respectively. (g, h) Misorientation angle distributions and (i) grain size distributions of as-built 316L-Si and 316L samples.

Figure 1a and b depict the EBSD inverse pole figures (IPFs) from the top areas (underneath and including the last added layer) of two as-built samples. Both materials exhibit many zigzag grain structures (marked by black arrows in Figure 1a, b) along the building direction with an inclination along the printing direction that is determined by the bidirectional scanning strategy. The maximum texture intensities in their pole figures (PFs) are 2.65 and 3.24 multiples of uniform density (MUD) (Figure 1c, d) for 316L-Si and 316L, respectively, showing a weak texture in their microstructures. In the case of 316L-Si, a large length fraction of ∑3 twin boundaries (up to 23%), prevail across all areas, as shown in Figure 1e and S1. Meanwhile, in 316L, only a limited number of ∑3 twin boundaries (2.25%) are evident across all areas (Figure 1f). This difference is reinforced through their corresponding misorientation angle distribution maps (Figure 1g, h). Furthermore, there is a significant decrease in mean grain size from 18.76

μm in 316L to 10.94 μm in 316L-Si (Figure 1i). Similar microstructures are found in the middle and bottom areas of printed parts along the building direction for both alloys (Figure S1).

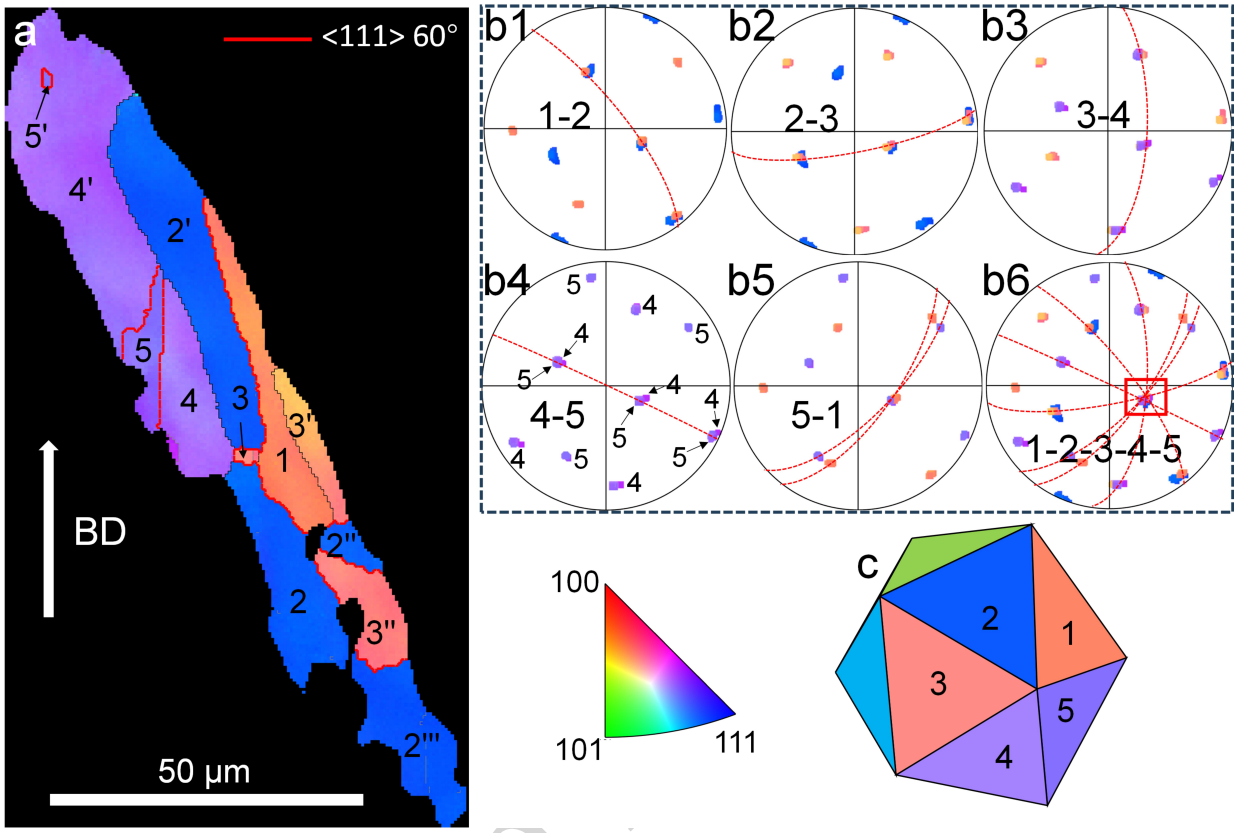

Figure 2. (a) EBSD IPF (along BD) map of five nearest-neighbor grains with multiple-twin relationships, which are selected from the top surface of the 316L-Si sample, as highlighted by a small black dotted rectangle in Figure 1a. (b1-5) <110> PFs of grain pairs 1-2, 2-3, 3-4, 4-5 and 5-1, where the red dashed circles show a {111} twin plane and the same grain colors are used as in (a). (b6) The combined <110> PF of grains 1-5 showing a common <110> fivefold symmetry axis, marked by a red rectangular box. (c) Schematic of the hypothetical icosahedral nucleus showing the mutual orientation relations of the five grains, employing the same colors used in (a). Grains 2, 2', 2'' and 2''', grains 3, 3', and 3'', grains 4 and 4', and grains 5 and 5' have similar orientations with misorientations less than 5°, which may be interconnected underneath (or above (before polishing)) the observed surface, as suggested by serial section EBSD in Figure S3.

Nearly all ∑3 twin boundaries observed in as-built 316L-Si display some non-zero curvature, which does not conform to the lenticular morphology of deformation twins [22]. Furthermore, these twins are not annealing twins, which could arise due to the solid-state thermal cycling occurring during printing a layer or adding more layers. The evidence is as follows: 1) if these twins were produced by thermomechanical cycling, then few or no twins should be found on the topmost layer, which only experiences cooling to room temperature after deposition. However, a large number of ∑3 twins are observed near the top (Figure 1e) and their fractions are similar to those in the middle and bottom layers (Figure S1). 2) L-DED 316L takes ~1 hour

to reach a fully recrystallized microstructure when annealed at 1000 °C [36]; however, the time for cyclic heat treatment above 1000 °C is of the order of milliseconds [29,37], which is not long enough to form the observed twin boundary lengths (Figure 1e). 3) The twin boundaries in annealed AM 316L are long straight ones [20,21] unlike the curved ones reported in this work. To reinforce this conclusion, a single line was printed using 316L-Si (Figure S2a), which experienced solidification and cooling down to room temperature. EBSD maps in the middle and end (Figure S2b-e) sections of the line reveal a significant presence of ∑3 twin boundaries. Hence, the formation of twins is predominantly attributed to solidification and the first cooling down to room temperature but not the subsequent solid-state thermal cycling.

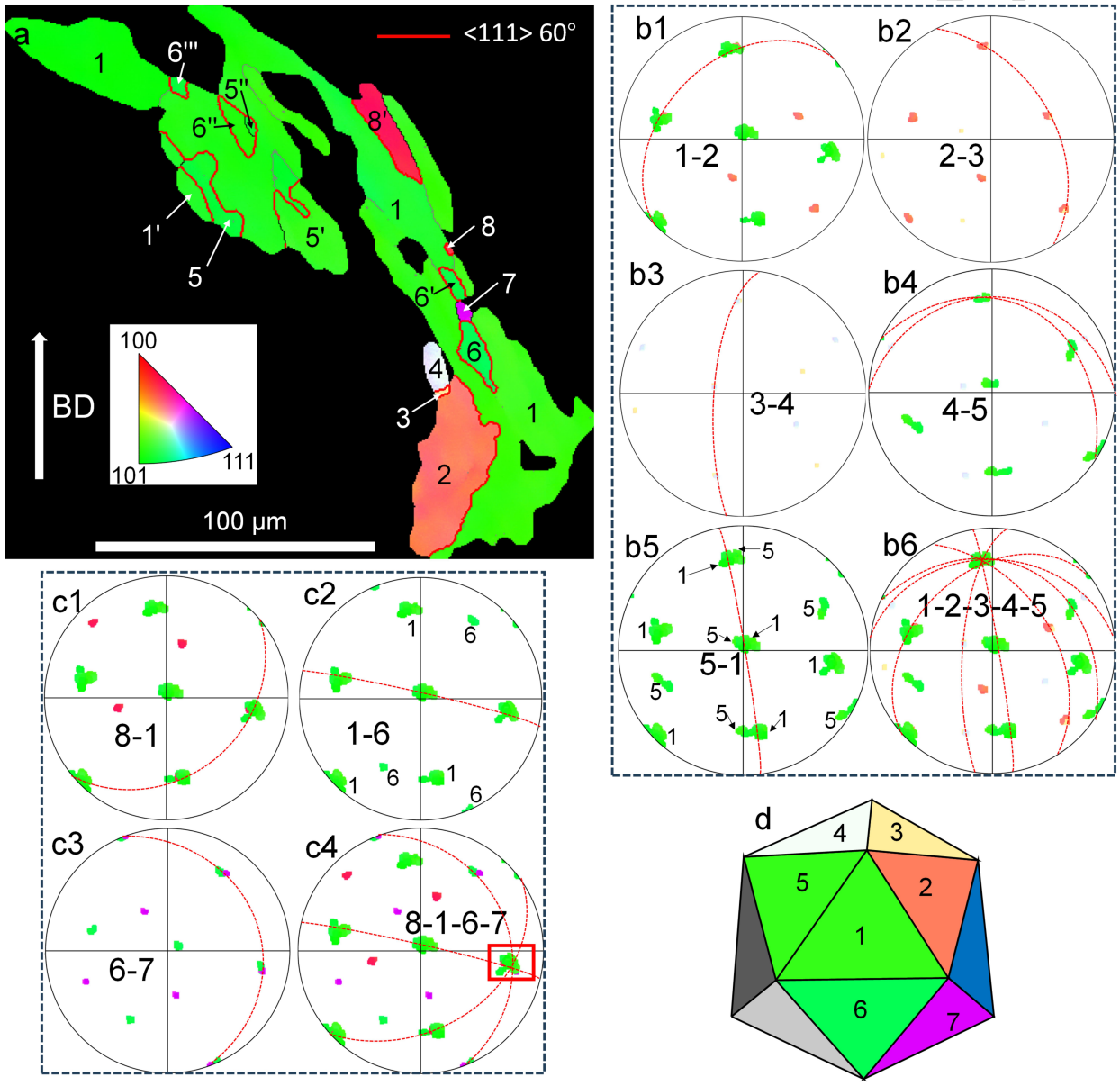

Figure 3. (a) EBSD IPF (along BD) map of a cluster of nearest-neighbor grains with multiple-twin relationships, which are selected from middle surface, as highlighted by a small back dotted

rectangle in Figure S1a. (b1-5) <110> PFs of grain pairs 1-2, 2-3, 3-4, 4-5 and 5-1, where the red dashed circle show a {111} twin plane and the same grain colors are used as in (a). (b6) The combined <110> PF of grains 1-5 showing a common <110> fivefold symmetry axis. (c1-4) <110> PFs of grains 1 and 6-8 showing a common <110> fivefold symmetry axis. (d) Schematics of hypothetical icosahedral nuclei showing the mutual orientation relations of grains 1-7, employing the same colors as (a). It is impossible to display grain 8 in (d) since only a maximum of three twin variants of grain 1 are allowed within one icosahedron.

In the following, arguments are provided to support the existence of some twin-related domains (TRDs) forming through ISRO-mediated nucleation.

Figure 2a shows a TRD in which a cluster of 5 neighboring grains (1–5) are connected by twin boundaries and exhibit a common <110> fivefold symmetry axis (Figure 2b1-6), clearly demonstrating the occurrence of ISRO-mediated nucleation; note that grains 2', 2" and 2"', grains 3', and 3", grain 4', and grain 5' have orientations similar (within 5° misorientation) to their non-prime counterparts. As shown in Figure 2(a, b1-4), grain pairs 1-2, 2-3, 3-4 and 4-5 have perfect twin relationships, but not 5-1 since their close {111} planes are rotated slightly along the common <110> direction (Figure 2b5). If grain pair 5-1 were to show a perfect twin relationship, then the sum of the angles between the normals to adjacent {111} planes around the common <110> direction of the five tetrahedra would be 352.5º [30]. However, the cumulated angle must be 360º. In theory, this difference can only be moderated by a rotation of 7.5º [23] around the common <110> direction of grain pair 5-1, which occurs through the near-twin relationship between grains 5 and 1.

Figure 3 shows another evidence of ISRO-mediated nucleation. Grain pairs 1-2, 2-3, 3-4 and 5-1 exhibit perfect twin relationships, and grain pair 4-5 presents a near-twin relationship (Figure 3); the same reasoning used for TRDs in Figure 2 can be applied here.

Similar to grains in Figure 2a, Figure 3a shows that grains 1 and 5 appear in a sequence of 1-5-1-5'-1-5", and grains 1 and 6 in a sequence of 1-6-1-6'-1-6"-1-6"', in which grains 5, 5' and 5", and grains 6, 6', 6" and 6"' have similar orientations with misorientations less than 5°. These grains are probably interconnected with each other underneath (or above (before polishing)) the observed surface (see serial section EBSD in Figure S3 and corresponding discussion).

Of all the observed TRDs in 316L-Si, only 3.1% show <110> fivefold symmetry axes on the studied surface (Figure S4); indeed, it is possible that this percentage is higher due to some grains contributing to clusters with <110> fivefold symmetry axes being present underneath the studied surface (or removed by polishing from above). Therefore, the 3.1% should be taken as a lower bound for the fraction of TRDs due to ISRO-mediated nucleation. In addition, grain growth may not be possible for all 20 faces to be observed with EBSD. Meanwhile, the significantly lower fraction of TRDs in 316L suggests that the amount of ISRO-based nucleation occurring in this steel is considerably lower, if not absent.

Redrawing attention to Figure 3, four twin variants of grain 1, namely, grains 2, 5, 6 and 8, are found. It is geometrically impossible for four twin variants to fit within the same icosahedron together. Apart from grains 1-5, which share a common <110> fivefold symmetry axis (Figure 3d), grains 1, 6, 7 and 8, with multiple-twin relationships (Figure 3c1-3), also share

a common <110> fivefold symmetry axis (with one orientation missing on the observed plane), as shown in Figure 3c4. This phenomenon cannot be explained from ISRO-mediated nucleation elucidated in Rappaz *et al*. [23]. Therefore, there must be other mechanism(s) involved during solidification or cooling down in the solid-state that should contribute to the formation of TRDs.

The solidification mode of stainless steel is determined by its equivalent chromium to equivalent nickel ratio (Cr_{eq}/Ni_{eq}). Following Suutala *et al.* [38], Cr_{eq}/Ni_{eq} is computed as:

$$(Cr + Mo + 1.5Si + 0.5Nb + 2Ti)/[Ni + 30C + 30(N - 0.06) + 0.5Mn](wt\ \%) \quad (1)$$

Based on this formula, the Cr_{eq}/Ni_{eq} of 316L and 316L-Si samples are 1.46 and 1.73, respectively. Recalling that the same printing parameters were used during L-DED for both 316L and 316L-Si, the solidification rates during fabrication are expected to be similar (if not the same due to compositional differences). Then, based on Cr_{eq}/Ni_{eq} of 316L and the typical solidification rates encountered during L-DED, it can solidify via A (primary austenite without ferrite) or AF (primary austenite with ferrite) modes [39,40]. However, with a Cr_{eq}/Ni_{eq} of 1.73, 316L-Si should solidify via either FA (primary ferrite with secondary austenite solidifying in the melt), F/MA (primary ferrite solidification followed by a massive transformation into austenite in the solid state) or Ferrite + Widmanstätten austenite modes [40,41]. Since Widmanstätten austenite is not found in our 316L-Si, the last mode can be excluded.

For solidification rates greater than 10 mm/s and Cr_{eq}/Ni_{eq} between 1.5 and 1.9, F/MA mode is reportedly predominant [40–43]. As stated in Brooks and Thompson [43], during F/MA, ferrite solidifies first and then massively transforms into austenite via thermally activated nucleation and growth with driving forces and atomic mobilities that are in between those of diffusional and shear transformations. It occurs without long-range diffusion and without the formation of solute segregation cells, which are typical during primary austenite solidification modes. Furthermore, they involve the motion of disordered interfaces with many facets [43]. In the L-PBF 316L studied by Monier [41], a "fish-scale" structure was reported involving microsegregation cells due to fully austenite (A) solidification mode and segregation-free regions due to F/MA mode. The combination of these two modes was attributed to the Cr_{eq}/Ni_{eq} (1.55) falling in the aforementioned range and spatially-varying solidification rates during L-PBF. A large length fraction of ∑3 twin boundaries were found mostly in segregation-free regions and were attributed to F/MA mode [41]. Similar phenomena were reported in other stainless steels after pulsed laser welding [40] and electron beam welding [44].

In what follows, we provide arguments in support of the predominant occurrence of the F/MA mode in 316L-Si: (i) Austenite is found to be the dominant phase in our 316L-Si. (ii) The average grain size is smaller in 316L-Si than in 316L (Figure 1i), which was printed using the same parameters. (iii) Solute segregation cells such as those occurring in 316L (Figure S5a) are not present in 316L-Si (Figure S5b). (iv) Jagged GBs are present between austenite grains (Figure 4a) [43]. Similar observations of refined grains, absence of solidification cells and jagged boundaries between austenite grains were reported by Inoue *et al*. [42] and Brooks and

Thompson [43] in their stainless steel welds and more recently by Monier [41] for their L-PBF 316L, in support of the occurrence of the F/MA mode.

Furthermore, lathy ferrites are found in the 316L-Si microstructure (Figure S5) and 25.2% of the ferrite/austenite boundaries are Kurdjumov-Sachs (KS) boundaries, observed even in neighboring twins (Figure 4a and b). While the presence of lathy ferrites could be justified either via F/MA or FA modes, Brooks and Thompson [43] argued that the presence of some ferrites in the predominantly austenite matrix indicates that massive transformation has occurred at high temperatures, leaving some time for short range diffusion to occur and form lathy ferrites with Mo, Cr and Si segregations (Figure 4c). Due to the rapid cooling rate during this process, a non-negligible number of ferrites precipitate along the low-energy K-S interfaces. In addition, during L-DED of 316L-Si, the long period of solid-state thermal cycling until the end of building should provoke additional diffusion that contributes to the formation of lathy ferrites that precipitate across high-energy non-KS interfaces.

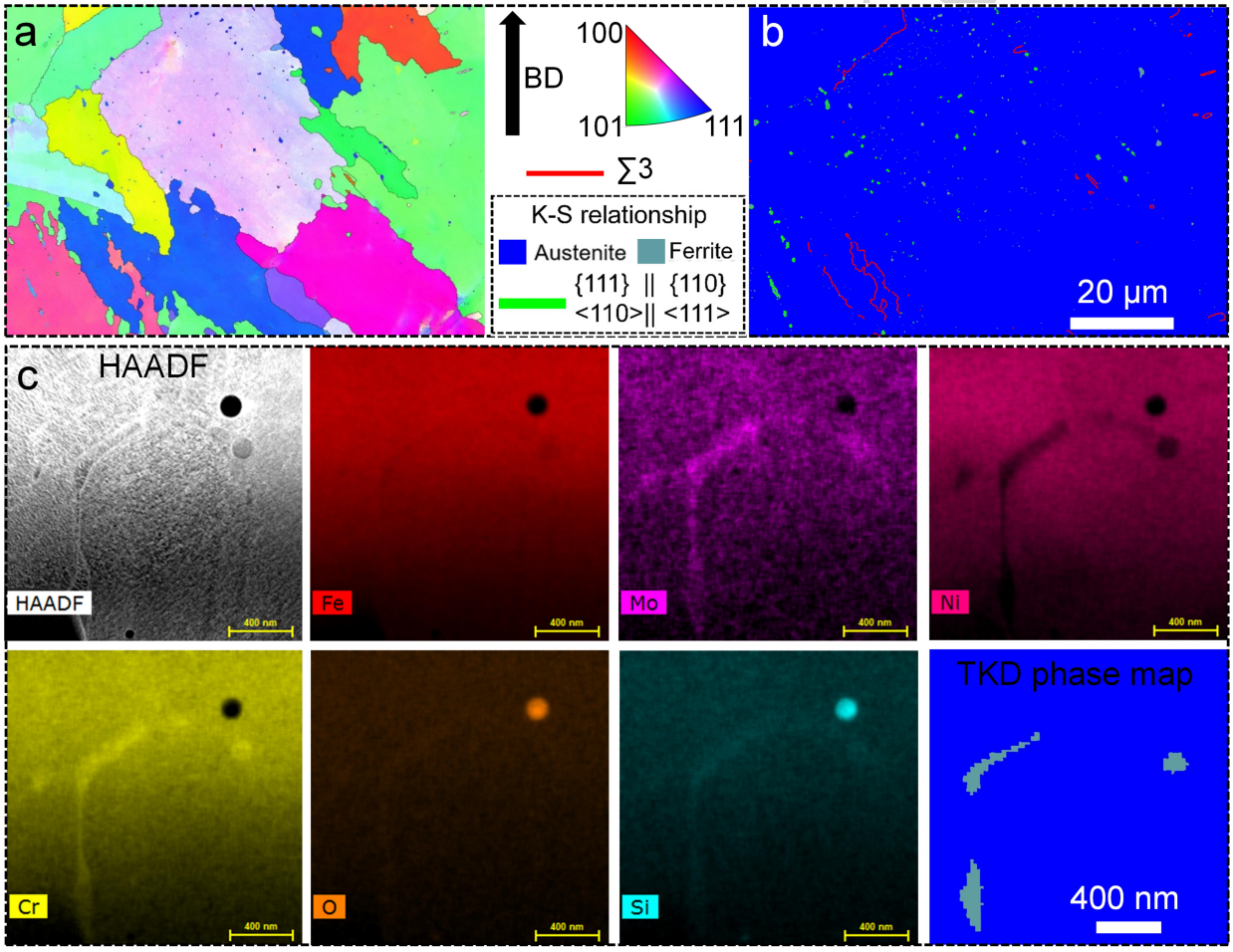

Figure 4. As-built 316L-Si: (a) IPF map (near the top of the as-built sample) along BD with a scanning step of 0.15 µm and (b) EBSD phase map (same zone as in (a)) superimposed by K-S and twin boundaries. (c) STEM HAADF image and EDS and TKD phase maps of ferrites in austenite matrix.

The presence of a larger length fraction of ∑3 twin boundaries in 316L-Si than in 316L is also a consequence of the F/MA mode. A possible explanation for the twin formation mechanism during such massive transformations was proposed by Aaronson et al. [45] based on the growth-accident model proposed by Gleiter *et al.* [46] and Mahajan *et al.* [47]. When the terrace plane of ledges along the misfit ferrite/austenite boundaries aligns with the habit plane of a twin, growth accidents may occur at these planes as successive growth ledges pass through, leading to the generation of Shockley-partial dislocations [45]. The repulsion between these partial dislocations facilitates the formation of micro-twins, which could eventually thicken to form macroscopic twins when a long and uninterrupted sequence of monoatomic ledges is present. It is worth noting that multiple twins can form during the migration of ferrite/massive-austenite boundaries [42], similar to the formation of TRDs in recrystallized FCC alloys [46,47].

In summary, this study demonstrates that the number of twin boundaries can be increased in 316L fabricated via L-DED by increasing the Si content, which provokes ISRO-mediated nucleation and F/MA solidification mode that are conducive to twin formation. Additional experiments need to be conducted in order to study whether the contribution of these mechanisms can be altered in order to generate the same number of twins or more. More broadly, this study underlines how standard alloy compositions can be altered to yield significant and desirable microstructural changes during AM.

Acknowledgments

The authors are grateful to Prof. Marie A. Charpagne for insightful discussions. KC, JGSM and MVU are grateful to the European Research Council (ERC) for their support through the European Union's Horizon 2020 research and innovation program for project GAMMA (Grant agreement No. 946959). The authors acknowledge the support of Simon Hallais (LMS, Ecole Polytechnique) for his guidance in training KC to use the SEM machine.

References

[1] Y.M. Wang, T. Voisin, J.T. McKeown, J. Ye, N.P. Calta, Z. Li, Z. Zeng, Y. Zhang, W. Chen, T.T. Roehling, R.T. Ott, M.K. Santala, P.J. Depond, M.J. Matthews, A.V. Hamza, T. Zhu, Additively manufactured hierarchical stainless steels with high strength and ductility, Nat. Mater. 17 (2018) 63–71. https://doi.org/10.1038/nmat5021.

[2] F. He, C. Wang, B. Han, G. Yeli, X. Lin, Z. Wang, L. Wang, J. Kai, Deformation faulting and dislocation-cell refinement in a selective laser melted 316L stainless steel, Int. J. Plast. 156 (2022) 103346. https://doi.org/10.1016/j.ijplas.2022.103346.

[3] L. Liu, Q. Ding, Y. Zhong, J. Zou, J. Wu, Y.-L. Chiu, J. Li, Z. Zhang, Q. Yu, Z. Shen, Dislocation network in additive manufactured steel breaks strength–ductility trade-off, Mater. Today 21 (2018) 354–361. https://doi.org/10.1016/j.mattod.2017.11.004.

[4] X. Zhang, P. Kenesei, J.-S. Park, J. Almer, M. Li, In situ high-energy X-ray study of deformation mechanisms in additively manufactured 316L stainless steel, J. Nucl. Mater. 549 (2021) 152874. https://doi.org/10.1016/j.jnucmat.2021.152874.

[5] C. Bean, F. Wang, M.A. Charpagne, P. Villechaise, V. Valle, S.R. Agnew, D.S. Gianola, T.M. Pollock, J.C. Stinville, Heterogeneous slip localization in an additively manufactured 316L stainless steel, Int. J. Plast. 159 (2022) 103436. https://doi.org/10.1016/j.ijplas.2022.103436.
[6] D.N. Wasnik, V. Kain, I. Samajdar, B. Verlinden, P.K. De, Effects of overall grain boundary nature on localized corrosion in austenitic stainless steels, Mater. Sci. Forum 467–470 (2004) 813–818. https://doi.org/10.4028/www.scientific.net/MSF.467-470.813.
[7] T. Liu, S. Xia, Q. Bai, B. Zhou, Y. Lu, T. Shoji, Evaluation of grain boundary network and improvement of intergranular cracking resistance in 316L stainless steel after grain boundary engineering, Materials 12 (2019) 242. https://doi.org/10.3390/ma12020242.
[8] D.N. Wasnik, V. Kain, I. Samajdar, B. Verlinden, P.K. De, Resistance to sensitization and intergranular corrosion through extreme randomization of grain boundaries, Acta Mater. 50 (2002) 4587–4601. https://doi.org/10.1016/S1359-6454(02)00306-3.
[9] D.C. Crawford, G.S. Was, The role of grain boundary misorientation in intergranular cracking of Ni-16Cr-9Fe in 360 °C argon and high-purity water, Metall. Trans. A 23 (1992) 1195–1206. https://doi.org/10.1007/BF02665051.
[10] A. Telang, A.S. Gill, M. Kumar, S. Teysseyre, D. Qian, S.R. Mannava, V.K. Vasudevan, Iterative thermomechanical processing of alloy 600 for improved resistance to corrosion and stress corrosion cracking, Acta Mater. 113 (2016) 180–193. https://doi.org/10.1016/j.actamat.2016.05.009.
[11] S. Kobayashi, R. Kobayashi, T. Watanabe, Control of grain boundary connectivity based on fractal analysis for improvement of intergranular corrosion resistance in SUS316L austenitic stainless steel, Acta Mater. 102 (2016) 397–405. https://doi.org/10.1016/j.actamat.2015.08.075.
[12] V.Y. Gertsman, S.M. Bruemmer, Study of grain boundary character along intergranular stress corrosion crack paths in austenitic alloys, Acta Mater. 49 (2001) 1589–1598. https://doi.org/10.1016/S1359-6454(01)00064-7.
[13] E.A. West, G.S. Was, IGSCC of grain boundary engineered 316L and 690 in supercritical water, J. Nucl. Mater. 392 (2009) 264–271. https://doi.org/10.1016/j.jnucmat.2009.03.008.
[14] L. Tan, T.R. Allen, J.T. Busby, Grain boundary engineering for structure materials of nuclear reactors, J. Nucl. Mater. 441 (2013) 661–666. https://doi.org/10.1016/j.jnucmat.2013.03.050.
[15] C. Hu, S. Xia, H. Li, T. Liu, B. Zhou, W. Chen, N. Wang, Improving the intergranular corrosion resistance of 304 stainless steel by grain boundary network control, Corros. Sci. 53 (2011) 1880–1886. https://doi.org/10.1016/j.corsci.2011.02.005.
[16] M. Shimada, H. Kokawa, Z.J. Wang, Y.S. Sato, I. Karibe, Optimization of grain boundary character distribution for intergranular corrosion resistant 304 stainless steel by twin-induced grain boundary engineering, Acta Mater. 50 (2002) 2331–2341. https://doi.org/10.1016/S1359-6454(02)00064-2.
[17] N. Bozzolo, M. Bernacki, Viewpoint on the formation and evolution of annealing twins during thermomechanical processing of FCC metals and alloys, Metall. Mater. Trans. A 51 (2020) 2665–2684. https://doi.org/10.1007/s11661-020-05772-7.
[18] K. Chen, H. Li, C.H. Lim, N. Jia, W. Yan, Fine grains within narrow temperature range by tuning strain-induced boundary migration dominated recrystallization for selective laser melted Inconel 718, Scr. Mater. 219 (2022) 114882. https://doi.org/10.1016/j.scriptamat.2022.114882.

[19] K. Chen, D.J. Huang, H. Li, N. Jia, W. Chong, Avoiding abnormal grain growth when annealing selective laser melted pure titanium by promoting nucleation, Scr. Mater. 209 (2022) 114377. https://doi.org/10.1016/j.scriptamat.2021.114377.
[20] T. Voisin, J.-B. Forien, A. Perron, S. Aubry, N. Bertin, A. Samanta, A. Baker, Y.M. Wang, New insights on cellular structures strengthening mechanisms and thermal stability of an austenitic stainless steel fabricated by laser powder-bed-fusion, Acta Mater. 203 (2021) 116476. https://doi.org/10.1016/j.actamat.2020.11.018.
[21] D. Kong, C. Dong, X. Ni, L. Zhang, J. Yao, C. Man, X. Cheng, K. Xiao, X. Li, Mechanical properties and corrosion behavior of selective laser melted 316L stainless steel after different heat treatment processes, J. Mater. Sci. Technol. 35 (2019) 1499–1507. https://doi.org/10.1016/j.jmst.2019.03.003.
[22] L. Monier, M. Buttard, M. Veron, J.-J. Blandin, G. Martin, F. Villaret, Y. Shen, B. Yrieix, C. Ernould, J. Guyon, A. Despres, On the origin of grain refinement and twin boundaries in as-fabricated austenitic stainless steels produced by laser powder bed fusion, Addit. Manuf. 61 (2023) 103351. https://doi.org/10.1016/j.addma.2022.103351.
[23] M. Rappaz, Ph. Jarry, G. Kurtuldu, J. Zollinger, Solidification of metallic alloys: Does the structure of the liquid matter?, Metall. Mater. Trans. A 51 (2020) 2651–2664. https://doi.org/10.1007/s11661-020-05770-9.
[24] J. Zollinger, B. Rouat, J. Guyon, S.K. Pillai, M. Rappaz, Influence of Ir additions and icosahedral short range order (ISRO) on nucleation and growth kinetics in Au-20.5Wt Pct Cu-4.5Wt PctAg alloy, Metall. Mater. Trans. A 50 (2019) 2279–2288. https://doi.org/10.1007/s11661-019-05176-2.
[25] M. Buttard, G. Martin, X. Bataillon, G. Renou, P. Lhuissier, J. Villanova, B. Chehab, P. Jarry, J.-J. Blandin, P. Donnadieu, Towards an alloy design strategy by tuning liquid local ordering: What solidification of an Al-alloy designed for laser powder bed fusion teaches us, Addit. Manuf. 61 (2023) 103313. https://doi.org/10.1016/j.addma.2022.103313.
[26] C. Galera-Rueda, M.L. Montero-Sistiaga, K. Vanmeensel, M. Godino-Martínez, J. Llorca, M.T. Pérez-Prado, Icosahedral quasicrystal-enhanced nucleation in Al alloys fabricated by selective laser melting, Addit. Manuf. 44 (2021) 102053. https://doi.org/10.1016/j.addma.2021.102053.
[27] C. Galera-Rueda, X. Jin, J. LLorca, M.T. Pérez-Prado, Icosahedral quasicrystal enhanced nucleation in commercially pure Ni processed by selective laser melting, Scr. Mater. 211 (2022) 114512. https://doi.org/10.1016/j.scriptamat.2022.114512.
[28] Y. Nie, Y.T. Chang, M.A. Charpagne, Origins of twin boundaries in additive manufactured stainless steels, Acta Mater. 275 (2024) 120035. https://doi.org/10.1016/j.actamat.2024.120035.
[29] M.V. Upadhyay, M.B.H. Slama, S. Gaudez, N. Mohanan, L. Yedra, S. Hallais, E. Héripré, A. Tanguy, Non-oxide precipitates in additively manufactured austenitic stainless steel, Sci. Rep. 11 (2021) 10393. https://doi.org/10.1038/s41598-021-89873-2.
[30] U. Scipioni Bertoli, B.E. MacDonald, J.M. Schoenung, Stability of cellular microstructure in laser powder bed fusion of 316L stainless steel, Mater. Sci. Eng. A 739 (2019) 109–117. https://doi.org/10.1016/j.msea.2018.10.051.
[31] G. Kurtuldu, P. Jarry, M. Rappaz, Influence of Cr on the nucleation of primary Al and formation of twinned dendrites in Al–Zn–Cr alloys: Can icosahedral solid clusters play a role?, Acta Mater. 61 (2013) 7098–7108. https://doi.org/10.1016/j.actamat.2013.07.056.

[32] T. Schenk, D. Holland-Moritz, V. Simonet, R. Bellissent, D.M. Herlach, Icosahedral short-range order in deeply undercooled metallic melts, Phys. Rev. Lett. 89 (2002) 075507. https://doi.org/10.1103/PhysRevLett.89.075507.
[33] B. Cordero, V. Gómez, A.E. Platero-Prats, M. Revés, J. Echeverría, E. Cremades, F. Barragán, S. Alvarez, Covalent radii revisited, Dalton Trans. (2008) 2832–2838. https://doi.org/10.1039/B801115J.
[34] M. Han, G.J. Miller, An application of the "coloring problem": structure−composition−bonding relationships in the magnetocaloric materials $LaFe_{13-x}Si_x$, Inorg. Chem. 47 (2008) 515–528. https://doi.org/10.1021/ic701311b.
[35] M. Akbari, R. Kovacevic, An investigation on mechanical and microstructural properties of 316LSi parts fabricated by a robotized laser/wire direct metal deposition system, Addit. Manuf. 23 (2018) 487–497. https://doi.org/10.1016/j.addma.2018.08.031.
[36] Z. Yan, K. Zou, M. Cheng, Z. Zhou, L. Song, Revealing relationships between heterogeneous microstructure and strengthening mechanism of austenitic stainless steels fabricated by directed energy deposition (DED), J. Mater. Res. Technol. 15 (2021) 582–594. https://doi.org/10.1016/j.jmrt.2021.08.036.
[37] A. Edwards, D. Weisz-Patrault, É. Charkaluk, Analysis and fast modelling of microstructures in duplex stainless steel formed by directed energy deposition additive manufacturing, Addit. Manuf. 61 (2023) 103300. https://doi.org/10.1016/j.addma.2022.103300.
[38] N. Suutala, T. Takalo, T. Moisio, Ferritic-austenitic solidification mode in austenitic stainless steel welds, Metall. Trans. A 11 (1980) 717–725. https://doi.org/10.1007/BF02661201.
[39] J.W. Elmer, S.M. Allen, T.W. Eagar, Microstructural development during solidification of stainless steel alloys, Metall. Trans. A 20 (1989) 2117–2131. https://doi.org/10.1007/BF02650298.
[40] J.C. Lippold, Solidification behavior and cracking susceptibility of pulsed-laser welds in austenitic stainless steels, Weld. J. Weld. Res. Suppl. 73 (1994) 129–139. https://www.osti.gov/biblio/7167543.
[41] L. Monier, Process-microstructure-tensile properties relationships in the 316L austenitic stainless steel produced by additive manufacturing, (2023). https://theses.hal.science/tel-04430850.
[42] H. Inoue, T. Koseki, S. Ohkit, T. Tanak, Effect of solidification on subsequent ferrite-to-austenite massive transformation in an austenitic stainless steel weld metal, ISIJ Int. 13 (1995) 1248–1257. https://doi.org/10.2355/isijinternational.35.1248.
[43] J.A. Brooks, A.W. Thompson, Microstructural development and solidification cracking susceptibility of austenitic stainless steel welds, Int. Mater. Rev. 36 (1991) 16–44. https://doi.org/10.1179/imr.1991.36.1.16.
[44] J.W. Elmer, The influence of cooling rate on the microstructure of stainless steel alloys, Lawrence Livermore National Lab. (LLNL), Livermore, CA (United States), 1988. https://doi.org/10.2172/5678406.
[45] H.I. Aaronson, S. Mahajan, G.R. Purdy, M.G. Hall, Origins of internal structure in massive transformation products, Metall. Mater. Trans. A 33 (2002) 2347–2351. https://doi.org/10.1007/s11661-002-0358-0.
[46] H. Gleiter, The formation of annealing twins, Acta Metall. 17 (1969) 1421–1428. https://doi.org/10.1016/0001-6160(69)90004-2.

[47] S. Mahajan, C.S. Pande, M.A. Imam, B.B. Rath, Formation of annealing twins in f.c.c. crystals, Acta Mater. 45 (1997) 2633–2638. https://doi.org/10.1016/S1359-6454(96)00336-9.
[48] C.M. Barr, A.C. Leff, R.W. Demott, R.D. Doherty, M.L. Taheri, Unraveling the origin of twin related domains and grain boundary evolution during grain boundary engineering, Acta Mater. 144 (2018) 281–291. https://doi.org/10.1016/j.actamat.2017.10.007.